Monthly Notices of the ROYAL ASTRONOMICAL SOCIETY

MNRAS **526,** 2365–2376 (2023)
Advance Access publication 2023 September 22

https://doi.org/10.1093/mnras/stad2888

Light elements Na and Al in 58 bulge spheroid stars from APOGEE

B. Barbuy [1,2★] A. C. S. Friaça,[1★] H. Ernandes [2★] T. Moura [†] T. Masseron,[3] K. Cunha [4,5,6] V. V. Smith [7] D. Souto [8] A. Pérez-Villegas [9] S. O. Souza [1] C. Chiappini [10] A. B. A. Queiroz [10] J. G. Fernández-Trincado [11] P. da Silva [1] B. X. Santiago [12] F. Anders [13] R. P. Schiavon [14] M. Valentini [10] D. Minniti [15,16] D. Geisler [17,18,19] V. M. Placco [7] M. Zoccali [20,21] M. Schultheis [22] C. Nitschelm [23] T. C. Beers [24] and R. Razera [25]

Affiliations are listed at the end of the paper

Accepted 2023 September 17. Received 2023 September 17; in original form 2023 August 18

ABSTRACT

We identified a sample of 58 candidate stars with metallicity [Fe/H] $\lesssim -0.8$ that likely belong to the old bulge spheroid stellar population, and analyse their Na and Al abundances from Apache Point Observatory Galactic Evolution Experiment (APOGEE) spectra. In a previous work, we inspected APOGEE-Stellar Parameter and Chemical Abundance Pipeline abundances of C, N, O, Mg, Al, Ca, Si, and Ce in this sample. Regarding Na lines, one of them appears very strong in about 20 per cent of the sample stars, but it is not confirmed by other Na lines, and can be explained by sky lines, which affect the reduced spectra of stars in a certain radial velocity range. The Na abundances for 15 more reliable cases were taken into account. Al lines in the H band instead appear to be very reliable. Na and Al exhibit a spread in abundances, whereas no spread in N abundances is found, and we found no correlation between them, indicating that these stars could not be identified as second-generation stars that originated in globular clusters. We carry out the study of the behaviour of Na and Al in our sample of bulge stars and literature data by comparing them with chemodynamical evolution model suitable for the Galactic bulge. The Na abundances show a large spread, and the chemodynamical models follow the main data, whereas for aluminum instead, the models reproduce very satisfactorily the nearly secondary-element behaviour of aluminum in the metallicity range below [Fe/H] $\lesssim -1.0$. For the lower-metallicity end ([Fe/H < -2.5), hypernovae are assumed to be the main contributor to yields.

Key words: stars: abundances – Galaxy: abundances – Galaxy: bulge – Galaxy: evolution.

1 INTRODUCTION

The mix of stellar populations in the Galactic bulge includes relics of an early classical bulge, as made evident from RR Lyrae (Dékány et al. 2013, Savino et al. 2020), red clump stars (Kunder et al. 2020), metal-poor stars (Arentsen et al. 2020, Sestito et al. 2023), and very old globular clusters such as NGC 6522 (e.g. Barbuy et al. 2009, 2014, 2021; Fernández-Trincado et al. 2019). The metal-poor stellar population components have a metallicity peak at [Fe/H] ≈ -1.0, and there are traces of lower-metallicity stars – see surveys by Howes et al. (2016), Casey & Schlaufman (2015), the Pristine Inner Galaxy Survey (Arentsen et al. 2020), and the Chemodynamical Origins of Metal-poor Bulge Stars (Lucey et al. 2022). Metallicities of [Fe/H] ≈ -1.0 in the Galactic bulge are due to a fast chemical enrichment (Chiappini et al. 2011, Wise et al. 2012, Barbuy, Chiappini & Gerhard 2018a). Tumlinson (2010) suggests that half of the oldest stars in the Galaxy should be found in the Galactic bulge.

The great majority of bulge stars, instead, show two major metallicity peaks at [Fe/H] ≈ -0.4 and $+$ 0.3 (Ness et al. 2013; Zoccali et al. 2017; Rojas-Arriagada et al. 2020 – see also Barbuy et al. 2018a). Zoccali, Valenti & Gonzalez (2018) found that the metallicity peak at [Fe/H] ≈ -0.4 make up 48 per cent of the total stellar mass of the bulge, within the region $|l| < 10$ and $|b| < 9.5$, it is more axisymmetric than the metal-rich one, and their orbits do not follow the bar, and the remaining 52 per cent belong to the range of metal-rich stars.

Queiroz et al. (2020, 2021, and references therein) reported the mix of stellar populations in the bulge, including the presence of a bar-induced pseudo-bulge (e.g. Bensby et al. 2017) inner thin and thick disc, inner halo, as well as accreted components such as *Gaia–Enceladus–Sausage* (Belokurov et al. 2018; Helmi et al. 2018). Horta et al. (2021) and Fernández-Trincado et al. (2022b) summarize the multiple other dwarf galaxy remnants, and minor substructures, accreted during the early stages of the Galaxy formation.

Understanding the formation of the present composition and structure of the Galactic bulge has involved, at first, early building blocks that merged into a proto-Milky Way (MW), within the lambda-cold dark matter scenario (White & Rees 1978; White & Frenk 1991), and within which the oldest *in situ* stars and clusters were formed. This is the component that we are interested in.

★ E-mail: b.barbuy@iag.usp.br (BB); amancio.friaca@iag.usp.br (ACSF); heitor.ernandes@geol.lu.se (HE)
† Visitor to IAG, Universidade de São Paulo, Rua do Matão 1226, Cidade Universitária, São Paulo, SP 05508-900, Brazil

Table 1. Line list: log *gf* from VALD3 (Piskunov et al. 1995, Ryabchikova et al. 2015), Kurucz (1993), and NIST (Martin et al. 2002).

Species	λ (Å)	χ_{ex} (eV)	log *gf* (VALD3)	log *gf* (Kurucz)	log *gf* (NIST)	Notes
Na I	15992.450	4.284	− 0.800	–	–	Little sensitive to abundance
	16373.853	3.753	− 1.330	− 1.330	− 1.328	Faint line
	16388.858	3.754	− 1.030	− 1.030	− 1.027	Best line, but has a sky line for some stars
	16786.400	4.289	− 1.300	–	–	Good line, but faint and blend with tellurics
Al I	16718.957	4.085	0.290	0.152	0.220	
	16750.539	4.088		0.408	–	
	16763.359	4.087	− 0.524	− 0.550	− 0.480	

In Razera et al. (2022), a selection of 58 candidate stars to belong to the oldest Galactic bulge *in situ* component was identified. The selection was based on the study by Queiroz et al. (2020, 2021), that combined APOGEE samples with proper motions from the *Gaia* Early Data Release 3 (EDR3, Gaia Collaboration 2021). Their selection consists of stars with a large eccentricity, orbits confined to the bulge region, and with moderate to low metallicities of [Fe/H] < -0.8. This sample could be a representative of the field counterpart of the oldest globular clusters in the inner Galaxy, as identified in Pérez-Villegas et al. (2020).

In Razera et al. (2022), we adopted the non-calibrated stellar parameters from the APOGEE Stellar Parameter and Chemical Abundance Pipeline (ASPCAP; García-Pérez et al. 2013, 2016), and rederived the abundances of C, N, O, and Ce, and adopted the ASPCAP data release 17 (DR17) abundances of Mg, Al, Ca, and Si. In the present work, we focus on the odd-Z elements Na and Al.

In Section 2, the selection of our sample is described. The element abundances are verified in Section 3. In Section 4, the results are compared with literature data for bulge samples, and discussed. In Section 5, conclusions are drawn.

2 THE SAMPLE

The APOGEE (Majewski, Schiavon & Frinchaboy 2017) is part of the Sloan Digital Sky Survey III and IV (SDSS; Blanton et al. 2017), that carried out a spectroscopic survey of MW stars.

The cryogenic, multifibre (300 fibres) APOGEE spectrograph (Wilson et al. 2019) on the 2.5-m SDSS telescope (Gunn et al. 2006) at Apache Point Observatory surveyed the Northern Hemisphere (APOGEE-2N), and on the 2.5-m Irénée du Pont telescope at Las Campanas Observatory the Southern Hemisphere (APOGEE-2S) was observed.

Zasowski et al. (2013, 2017, 2019), Beaton et al. (2020), and Santana et al. (2021) give further details regarding the design of the APOGEE survey and target selections. The data reduction pipeline is described in Nidever et al. (2015), and the APOGEE line list is described in Smith et al. (2021), Cunha et al. (2017), and Hasselquist et al. (2016). The DR17 is the final data release of the SDSS-IV survey which ended in 2021 January. It contains high-resolution ($R \sim 22\,500$) near-infrared H-band spectra for over 2.6×10^6 stars, covering both northern and southern sky (Abdurro'uf et al. 2022).

In Razera et al. (2022), the selection of 58 spheroid bulge stars was described. In summary, we started from the chemo-orbital reduced-proper-motion sample selection carried out in Queiroz et al. (2021): orbits were computed adopting distances from StarHorse (Santiago et al. 2016; Queiroz et al. 2018), and proper motions from the *Gaia* EDR3 (Gaia Collaboration 2021). In order to identify spheroidal bulge stars, we adopted a maximum distance to the Galactic centre of $d_{GC} < 4$ kpc (Bica, Ortolani & Barbuy 2016); a maximum vertical excursion from the Galactic plane $|z|_{max} < 3.0$ kpc; eccentricity > 0.7; orbits that do not indicate a membership in the bar structure; counter-rotating stars azimuthal velocity ($V_\phi < 0.0$); and metallicities [Fe/H] < -0.80.

The coordinates, distance, proper motions, radial velocities, pericentric and apocentric distances, maximum height, and eccentricities of the 58 selected stars are given in Razera et al. (2022). Spectra have SNR > 50, and 56 out of the 58 stars show a renormalized unit weight error (RUWE) *Gaia* EDR3 parameter RUWE ≤ 1.4, therefore have reliable astrometric parameters.

3 ANALYSIS

The abundances were determined by comparing the observed spectra with the synthetic ones. The synthetic spectra are computed with the code TURBOSPECTRUM from Alvarez & Plez (1998) and Plez (2012). Model atmosphere grids are from Gustafsson et al. (2008). This code and model atmosphere grid is similar to the ASPCAP software, and therefore is suitable for comparisons.

Table 1 reports the lines that we verified in the spectra of the 58 sample stars. The atomic line list employed is that from the APOGEE collaboration described in Smith et al. (2021). Molecular electronic transition lines of CN $A^2\Pi$-$X^2\Sigma$ from Sneden et al. (2014) and Brooke et al. (2014), vibration-rotation CO $X^1\Sigma^+$ from Li et al. (2015), C_2 Ballik-Ramsay $b3\Sigma g^-$ - $a3\Pi u$ and Phillips $A1\Pi u$ - $X1\Sigma g^+$ from Yurchenko et al. (2018), and FeH $A^4\Delta$ - $X^4\Delta$ from Hargreaves et al. (2010) are included.

We have adopted the non-calibrated (spectroscopic) stellar parameters effective temperature $T_{\rm eff}$, gravity log g, metallicity [Fe/H], and microturbulence velocity v_t obtained through the ASPCAP (García-Pérez et al. 2016) software from DR17. These stellar parameters are reported in Table 2.

For the solar abundance of Na and Al, we adopt A(Na)= 6.17 and A(Al) = 6.37 from Grevesse, Asplund & Sauval (2007) and adopted by Smith et al. (2021), close to the values of A(Na)= 6.22 and A(Al) = 6.43 from Asplund, Amarsi & Grevesse (2021), and A(Na)= 6.33 and A(Al) = 6.47 from Grevesse & Sauval (1998).

For verification, we also computed all lines for all stars with the code PFANT (Barbuy et al. 2018b), as described in Razera et al. (2022), with the difference that we replaced the CO line list from Goorvitch (1994) with the one of Li et al. (2015).

3.1 Na and Al lines

Sodium

The Na I lines are weak, and a check of all four lines available in the APOGEE spectra is useful in order to avoid discrepancies. In particular, the line Na I 16388.850 Å appears very strong in a fraction of stars - see example in Fig. 1. Hayes et al. (2022) have

Table 2. Coordinates, stellar parameters, Na and Al abundances from original APOGEE-ASPCAP derivations from DR17 and [Al/Fe] for stars not available from DR17, and derived with TURBOSPECTRUM ([Al/Fe]T), using the lines reported in Table 1.

ID internal	ID 2MASS	α (deg)	δ (deg)	$T_{\rm eff}$ (K)	log g	[Fe/H]	v_t (km s^{-1})	[Na/Fe]	[Al/Fe]	[Al/Fe]T
b1	2M17153858−2759467	258.911	−27.996	3922.7	0.34	−1.65	2.62	0.25	− 0.13	− 0.27
c1	2M17173248−2518529	259.385	−25.315	3977.0	1.0	−0.91	1.81	− 0.13*	0.08	0.00
b2	2M17173693−2806495	259.404	−28.114	3908.9	0.95	−0.97	2.20	− 0.25	0.19	0.12
c9	2M17190320−2857321	259.763	−28.959	4139.6	1.19	−1.20	1.83	0.53	0.05	0.00
c10	2M17224443−2343053	260.685	−23.718	4058.3	1.02	−0.88	1.97	− 0.10*	0.38	0.23
b3	2M17250290−2800385	261.262	−28.011	3796.6	0.91	−0.82	2.39	− 0.06*	0.04	0.00
b4	2M17265563−2813558	261.732	−28.232	4096.2	1.0	−1.32	1.89	0.69	0.02	0.00
b5	2M17281191−2831393	262.050	−28.528	4029.1	0.96	−1.19	1.73	− 0.39	0.05	0.00
c2	2M17285088−2855427	262.212	−28.929	3838.0	0.63	−1.23	2.18	− 0.38	− 0.07	0.00
c15	2M17291778−2602468	262.324	−26.046	3844.3	0.71	−0.99	2.10	− 0.44	0.27	0.20
c11	2M17292082−2126433	262.337	−21.445	3983.4	0.78	−1.27	2.59	0.21	0.27	0.40
c25	2M17293482−2741164	262.395	−27.688	4143.5	1.03	−1.25	1.85	0.04	0.02	− 0.05
b6	2M17295481−2051262	262.478	−20.857	4205.9	1.50	−0.85	1.71	− 0.72	0.38	0.25
c3	2M17301495−2337002	262.562	−23.617	3814.0	0.69	−1.06	2.22	0.26	0.19	0.19
b7	2M17303581−2354453	262.649	−23.913	3863.0	0.77	−0.98	2.13	− 0.20	0.20	0.06
c16	2M17310874−2956542	262.786	−29.948	4175.7	1.20	−0.93	2.07	− 0.02	0.21	0.15
c12	2M17323787−2023013	263.158	−20.384	3865.7	1.03	−0.85	1.94	− 0.05	0.22	0.20
b8	2M17324257−2301417	263.177	−23.028	3668.2	0.79	−0.82	2.30	0.09/**0.25***	0.22	0.18
b9	2M17330695−2302130	263.279	−23.037	3566.6	0.35	−0.93	2.42	− 0.16	− 0.08	0.10
c13	2M17330730−2407378	263.280	−24.127	4042.5	0.25	−1.90	1.88	0.35	− 0.17	-0.31
c26	2M17341796−3905103	263.575	−39.086	4163.5	1.42	−0.89	1.84	− 0.28	0.35	0.35
c27	2M17342067−3902066	263.586	−39.035	4380.4	1.40	−0.93	1.99	0.36*	0.30	0.15
b10	2M17344841−4540171	263.702	−45.671	3869.2	0.85	−0.88	2.16	− 0.22*	0.27	0.10
b11	2M17351981−1948329	263.833	−19.809	3553.5	0.44	−1.11	3.06	− 0.15	− 0.01	− 0.05
b12	2M17354093−1716200	263.921	−17.272	3895.5	1.01	−0.87	2.02	− 0.20	0.24	0.18
c17	2M17382504−2424163	264.604	−24.405	3880.4	0.99	−1.05	1.55	0.26*	0.27	0.18
b13	2M17390801−2331379	264.783	−23.527	3740.4	0.83	−0.81	2.35	− 0.03/**0.25***	0.05	0.05
b14	2M17392719−2310311	264.863	−23.175	3643.3	0.67	−0.87	2.55	− 0.15*	− 0.06	0.05
c4	2M17453659−2309130	266.402	−23.154	4133.1	1.27	−1.20	1.08	− 0.15	− 0.12	− 0.15
b15	2M17473299−2258254	266.887	−22.974	4018.3	0.47	−1.74	2.12	0.15	− 0.11	− 0.25
b16	2M17482995−2305299	267.125	−23.092	4213.6	1.24	−1.03	2.10	0.06*	-0.06	− 0.20
b17	2M17483633−2242483	267.151	−22.713	3651.5	0.44	−1.09	2.58	-0.20/**0.08***	0.08	0.06
c28	2M17503065−2313234	267.628	−23.223	3819.4	0.98	−0.88	2.1	0.09*	0.23	0.28
b18	2M17503263−3654102	267.636	−36.903	3893.5	0.64	−0.99	2.19	0.08*	0.23	0.17
c18	2M17511568−3249403	267.815	−32.828	3921.2	0.98	−0.90	2.04	− 0.02	0.21	0.18
c5	2M17532599−2053304	268.358	−20.892	3896.9	0.91	−0.87	2.10	− 0.19	0.18	0.15
c19	2M17552681−3334272	268.862	−33.574	4051.0	1.08	−0.89	1.98	− 0.14	0.46	0.41
b19	2M17552744−3228019	268.864	−32.467	4018.9	1.0	−1.06	2.00	− 0.08	0.23	0.10
c20	2M18005152−2916576	270.215	−29.283	4158.9	1.04	−1.02	2.21	0.16	0.32	0.23
c21	2M18010424−3126158	270.268	−31.438	3773.1	0.68	−0.83	2.20	0.00/**0.02***	0.16	0.05
b20	2M18020063−1814495	270.503	−18.247	3988.8	0.80	−1.38	2.04	− 0.20	− 0.05	-0.20:
c14	2M18023156−2834451	270.632	−28.579	3617.4	0.42	−1.19	3.02	− 0.64	0.01	0.10
c22	2M18042687−2928348	271.112	−29.476	4164.7	0.88	−1.21	2.14	− 0.15	− 0.05	− 0.17
c6	2M18044663−3132174	271.194	−31.538	3832.6	0.92	−0.90	2.22	− 0.06	0.18	0.20
b21	2M18050452−3249149	271.269	−32.821	3940.8	0.77	−1.16	2.08	− 0.45	0.23	0.14
b22	2M18050663−3005419	271.278	−30.095	3439.9	0.23	−0.92	2.52	0.01*	− 0.08	− 0.02
c23	2M18052388−2953056	271.350	−29.885	4252.9	0.92	−1.57	1.92	0.57	− 0.03	− 0.20
b23	2M18065321−2524392	271.722	−25.411	3893.1	0.95	−0.89	2.02	− 0.73	0.27	0.20
c7	2M18080306−3125381	272.013	−31.427	4310.0	1.57	−0.90	1.48	− 0.70	0.46	0.50
b24	2M18104496−2719514	272.687	−27.331	4153.1	1.33	−0.82	2.05	− 0.05	0.25	0.12
b25	2M18125718−2732215	273.238	−27.539	3617.2	0.44	−1.31	2.64	− 0.31	− 0.21	− 0.30
c24	2M18142265−0904155	273.594	−9.071	3920.5	1.12	−0.85	2.13	− 0.32	0.29	0.18
c29	2M18143710−2650147	273.655	−26.837	4240.5	1.30	−0.92	1.97	− 0.20	0.26	0.13
c30	2M18150516−2708486	273.772	−27.147	3833.4	1.0	−0.83	2.14	− 0.04	0.24	0.14
c8	2M18195859−1912513	274.994	−19.214	4102.0	1.05	−1.24	1.78	− 0.16	0.02	0.00
b26	2M18200365−3224168	275.015	−32.405	3976.6	0.95	−0.86	1.94	− 0.05	0.35	0.22
c31	2M18344461−2415140	278.686	−24.254	4294.5	1.09	−1.42	1.83	− 0.23	0.12	− 0.03
b27	2M18500307−1427291	282.513	−14.458	4076.0	1.23	−0.95	1.73	− 0.10	0.31	0.15

Notes. [Na/Fe] values in bold face are from the VAC data derived with BAWLAS (see the text) and those marked with a star:* are the considered ones.

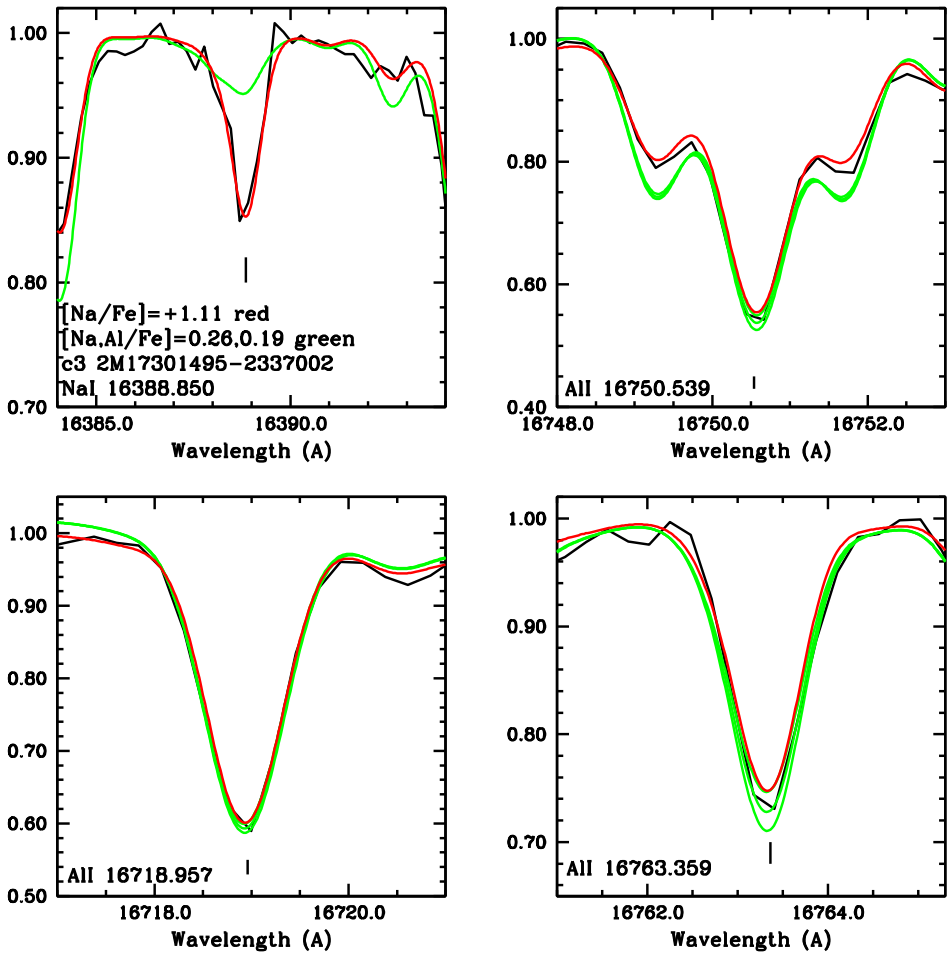

Figure 1. Na I 16388.850 Å, and the three Al I 16718.957, 16750.539, and 16763.359 Å lines in star 2M17301495−2337002. Observed spectrum (black) and synthetic spectra computed with [Na,Al] = 0.26,0.19 ± 0.10 (green), and [Na,Al] = 1.11,0.19 (red). Note that the higher Na abundance changes the strength of the also present CO, C_2 lines.

verified that stars with apparently strong Na I 16388 Å lines fall in the radial velocity range where a strong night sky line falls on this Na I line. This is due to a poor night sky line subtraction, for stars in the radial velocity range that should be avoided for this Na I line, which is about −60 to −110 km s^{-1}. This includes 14 stars from our sample, that we discarded for the Na abundance plot.

This is corroborated by the fact that the high Na abundance that would be needed to reproduce the line Na I 16388.850 Å is however not confirmed by the other Na lines, and in particular line Na I 16373.853 Å that has very similar excitation energy and oscillator strength, as illustrated in Fig. 2 showing that the high Na abundances are contradicted by another three Na I lines for star 2M17301495−2337002. On the other hand, among the stars in the radial velocity range to be discarded, star b17 = 2M17483633−2242483 shows the affected line giving Na abundances compatible with the other lines, and this one is kept.

Note also that the high Na abundances do affect the fit of the Al lines, due to the dissociation equilibrium involving several Na-composed molecules, such as NaO, NaC, NaOH, and NaAl, as shown in the subsection below.

The ASPCAP DR17 [Na/Fe] values are reported in Table 2. For four stars there are the verified and more reliable results based on the Value Added Catalogue (VAC) that were processed through the BACCHUS Analysis of weak lines in APOGEE spectra (BAWLAS; Hayes et al. 2022) and they are given in bold face in the table.

For the five more metal-poor stars the Na lines are too weak, therefore Na in these stars were also discarded.

Another check we carried out was to compare the fits from the ASPCAP Na abundances with the fits with TURBOSPECTRUM: abundances discrepant by more than ∼0.40 dex which led us to discard the Na abundance of another 16 stars.

Fig. 2 shows the fit to one of the best spectra as concerns the Na lines, fitted with the values issued from our calculations with TURBOSPECTRUM, the value from DR17, and the BAWLAS calibrated value. This figure shows that: (i) the Na I 15992.5 Å line is insensitive to the Na abundance;and (ii) the BAWLAS value is suitable with the local thermodynamic equilibrium (LTE) calculations even if it considered non-LTE (NLTE) effects.

Thus, we have considered the four BAWLAS analysed stars, and for these the Na abundance is close to the fits with TURBOSPECTRUM. This can be seen in Fig. 2, where the value [Na/Fe] = 0.25 from BAWLAS is compatible with that from TURBOSPECTRUM of [Na/Fe] = 0.36. We also considered the other 11 stars for which [Na/Fe] values from ASPCAP-DR17 and from TURBOSPECTRUM fits are compatible. In total, we are left with 15 stars with reliable Na abundances.

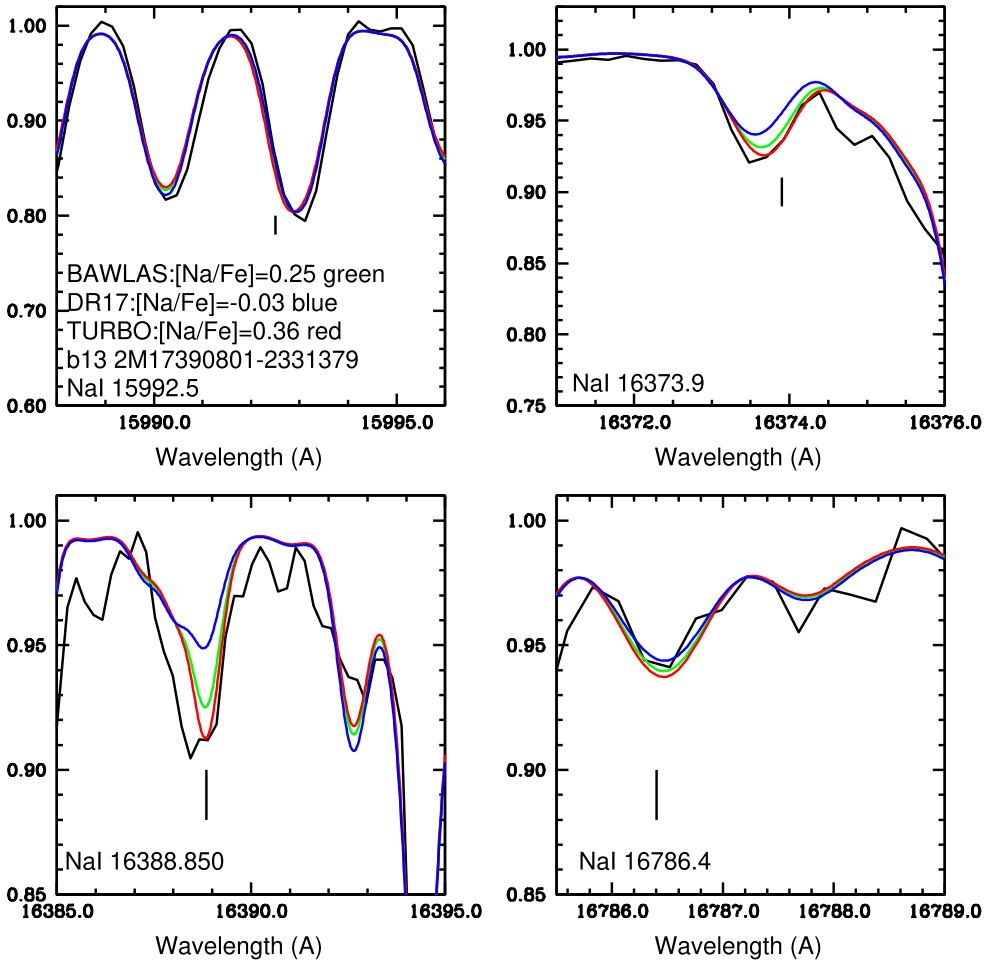

Figure 2. Star b13 = 2M17390801−2331379: observed spectrum (black) and synthetic spectrum computed with the results from TURBOSPECTRUM: [Na/Fe] = 0.36 (red), DR17: [Na/Fe] = −0.03, and BAWLAS: [Na/Fe] = 0.25 (green) showing the fit to the four Na lines.

As final comments on Na, Martell et al. (2016) preferred not to analyse Na from APOGEE. Jönsson et al. (2020) also point out that, after inspecting several Na lines, in APOGEE DR16, where Na is measured using only two relatively weak lines, they conclude that it is one of the least precisely determined element abundances. The technical problems with Na lines, in particular, in regions of tellurics, are also described in Jönsson et al. (2020). Finally, Osorio et al. (2020) point out NLTE effects in the H-band Na lines.

Aluminum

The Al abundances were derived with both the TURBOSPECTRUM and PFANT codes, and the results essentially correspond to the ASPCAP abundances, as can be seen in Table 2, where the TURBOSPECTRUM results are reported in the column [Al/Fe]T.

Fig. 1 shows the Na I 16388.850 Å feature, and the three Al I 16718.957, 16750.539, and 16763.359 Å lines for star 2M17301495−2337002. This figure illustrates the influence of the Na abundance on the strength of the Al lines, due to blends with C-, O-bearing molecular lines, that is, a higher Na abundance leads to formation of more NaC, NaOH, etc., therefore changing the dissociation equilibrium, and modifying the strength of CO, CN, C_2, and OH lines. This is shown by the red lines corresponding to the higher Na abundance that causes changes in the strength in the also present CO and C_2 lines.

The fits to all 58 stars for Al are suitable by adopting the ASPCAP abundances within 0.2 dex, and in most cases within 0.1 dex. Another example is given in Fig. 3 for star c1 = 2M17173248−2518529, for which [Na,Al] = 0.26,0.0 is adopted, whereas ASPCAP gives [Na,Al] = −0.13,0.08.

For Star b20 = 2M18020063−1814495 the fit to line Al I 16718.957 Å is stronger by about 0.2 dex, relative to the fit to the lines Al I 16750.539 and 16763.359 Å. The somewhat higher value from ASPCAP would aggravate the discrepancy for line Al I 16718.957 Å. This may be due to non-optimal stellar parameters for this rather cool red giant. For all other stars, the Al abundances are compatible within ±0.1 dex between the three Al lines.

Finally, NLTE corrections for the Al I 16718.957 and 16750.539 Å lines are provided by Nordlander & Lind (2017). The corrections for stars of metallicity [Fe/H] ∼ −1.0 and effective temperature near 4500 K are rather small.

4 RESULTS

The α-element abundances in bulge stars provide us with a constraint on the formation history of its stellar populations: the formation timescale. In other words, a mean [α/Fe] ∼ 0.5 in halo and bulge metal-poor stars of [Fe/H] $\lesssim -1.0$ indicates a fast chemical enrichment at

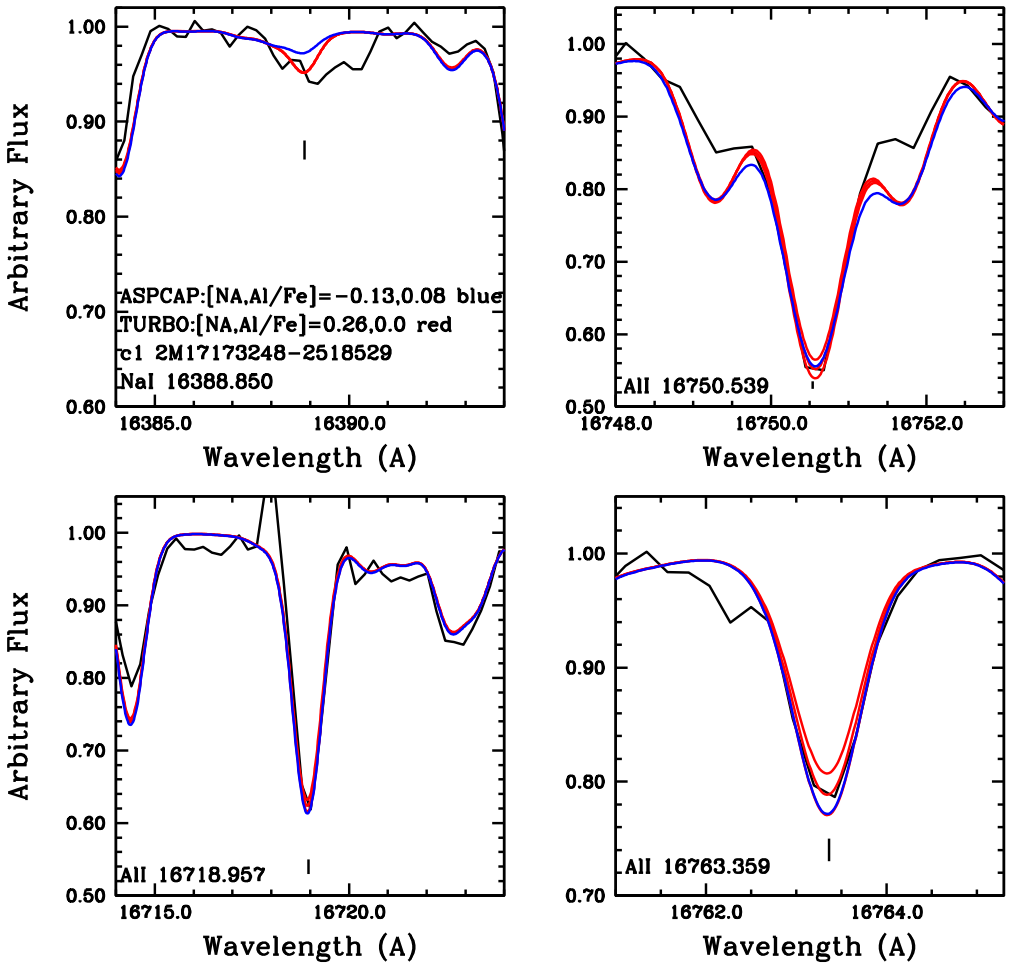

Figure 3. Na I 16388.850 Å, and the three Al I 16718.957, 16750.539, and 16763.359 Å lines in star c1 = 2M17173248−2518529. Observed spectrum (black) and synthetic spectra computed with the code TURBOSPECTRUM (red), adopting [Na,Al] = 0.26,0.0 ± 0.10 and with the very close ASPCAP abundances [Na,Al] = −0.13,0.08.

early times, dominated by supernovae type II (SNeII, Woosley & Weaver 1995).

4.1 Chemo-dynamical evolution models and the odd-Z elements Na and Al

The chemodynamical model is discussed in Friaça and Barbuy (2017) and Razera et al. (2022). In summary, the chemodynamical model is based on the model of galactic chemical evolution of Friaça & Terlevich (1998), consisting of a multizone chemical evolution coupled with a hydrodynamical code. For the Galactic bulge, a classical spheroid with a baryonic mass of 2×10^9 $M_\odot$, and a dark halo mass of 1.3×10^{10} $M_\odot$ are assumed. Cosmological parameters of $\Omega_m = 0.31$, $\Omega_\Lambda = 0.69$, Hubble constant $H_0 = 68$ km s^{-1} Mpc^{-1}, and age of the Universe of 13.801 ± 0.024 Gyr (Planck Collaboration 2020) are assumed.

For the nucleosynthesis yields, we adopt: (i) from massive stars, the metallicity dependent yields from core-collapse SNe (SNe II) from Woosley & Weaver (1995), with some alterations of the yields following the suggestions of Timmes, Woosley & Weaver (1995), and for low metallicities ($Z < 0.01$ $Z_\odot$, or Fe/H] < −2.5), the yields are from high explosion-energy hypernovae (HNe) from Nomoto, Kobayashi & Tominaga (2013); (ii) Type Ia SNe yields from Iwamoto et al. (1999) – their models W7 (progenitor star of initial metallicity $Z = Z_\odot$) and W70 (zero initial metallicity); and (iii) for intermediate-mass stars (0.8–8 $M_\odot$) with initial $Z = 0.001$, 0.004, 0.008, 0.02, and 0.4 yields are from van den Hoek and Groenewegen (1997; variable η asymptotic giant branch, AGB case).

In Fig. 4 are plotted the APOGEE ASPCAP DR17 values for 11 stars and the BAWLAS values for 4 stars. Literature data are from Alves-Brito et al. (2010), Bensby et al. (2017), Casey & Schlaufman (2015), Cunha & Smith (2006), Fulbright, McWilliam & Rich (2007), Howes et al. (2016), Johnson et al. (2014), Koch et al. (2016), Lamb et al. (2017), Lecureur et al. (2007), Rich et al. (2012), Ryde et al. (2016), and Siqueira-Mello et al. (2016). In this figure are overplotted the outputs of models computed for radii $r < 0.5$, $0.5 < r < 1$, $1 < r < 2$, and $2 < r < 3$ kpc from the Galactic centre, and for star formation rate (SFR) values of $\nu = 1$ and 3 Gyr^{-1}. The enhancement of α-elements in bulge red giants appears to require such fast SFRs, as discussed in Friaça & Barbuy (2017). Similar fast SFRs are adopted by, for example, Matteucci et al. (2020).

Here, $\nu = \nu_{SF}$ is the inverse of the time-scale for the system formation (given in Gyr^{-1}), that is, it is the ratio of the SFR over the gas mass in $M_\odot$ available for star formation, or $\nu_{SF} = 1/M(M_\odot)$ $dM(M_\odot)/dt$.

The Na abundance data show a large spread at all metallicities and from different sources and wavelength regions. Clearly the models do not reproduce a drop in Na abundance as seen from the APOGEE

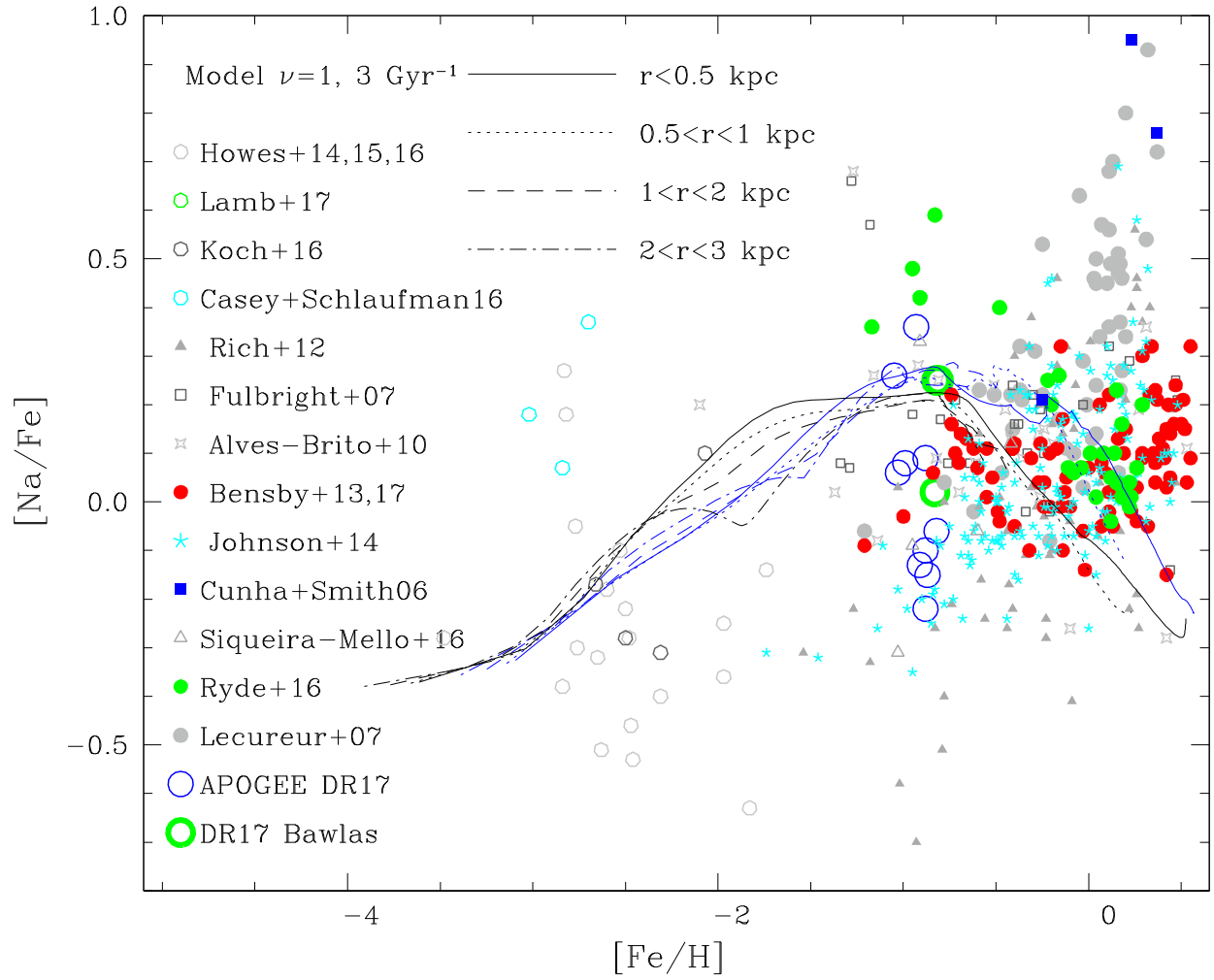

Figure 4. Na/Fe] versus [Fe/H] for literature bulge field stars and 11 APOGEE ASPCAP DR17 abundances, plus 4 BAWLAS abundances. Symbols: grey four-pointed stars: Alves-Brito et al. (2010); red filled circles: Bensby et al. (2017); blue filled squares: Cunha & Smith (2006); strong-grey filled triangles: Fulbright et al. (2007); grey open pentagons: Casey & Schlaufman (2015); grey open pentagons: Howes et al. (2016); grey stars: Johnson et al. (2014); grey open pentagons: Koch et al. (2016); green open pentagons: Lamb et al. (2017); dark grey filled circles: Lecureur et al. (2007); green filled circles: Ryde et al. (2016); grey open triangles: Siqueira-Mello et al. (2016); blue open circles: APOGEE ASPCAP DR17, and open green circles: BAWLAS. Chemodynamical evolution models with star formation rate of $\nu = 1\,\mathrm{Gyr}^{-1}$ (black) and $3\,\mathrm{Gyr}^{-1}$ (blue) or formation time-scale of 1 and 0.3 Gyr are overplotted. Different model lines correspond to the outputs of models computed for radii $r < 0.5$, $0.5 < r < 1$, $1 < r < 2$, and $2 < r < 3$ kpc from the Galactic centre.

data, and other literature data, and also it does not follow the increase in Na abundance at the metal-rich end. This latter point is important because strong Na features in galaxies have been used as argument to infer an initial mass function (IMF) top-heavy, that is, with more massive stars (e.g. Spiniello et al. 2012).

Models from Smiljanic et al. (2016), and Kobayashi, Karakas & Lugaro (2020) are applied to solar neighbourhood stars. Even so, these models as well as models from Kobayahi et al. (2006) applied to the Galactic bulge follow the same trends as the present models.

In Fig. 5 are plotted the APOGEE ASPCAP DR17 abundances for Al. Literature data are from Alves-Brito et al. (2010), Bensby et al. (2017), Casey & Schlaufman (2015), Fulbright et al. (2007), Howes et al. (2016), Johnson et al. (2014), Lamb et al. (2017), Ryde et al. (2016), and Siqueira-Mello et al. (2016). In this figure, we omitted the results from Lecureur et al. (2007) which appear out of scale and too spread. As in Fig. 4, the outputs of models computed for radii $r < 0.5$, $0.5 < r < 1$, $1 < r < 2$, and $2 < r < 3$ kpc from the Galactic centre are overplotted, and for the cases $\nu = 1$ and 3 Gyr^{-1}.

The steep decreasing trend of [Al/Fe] towards lower metallicities for the entire range $-4 < [\mathrm{Fe/H}] < -1$ is nicely predicted.

Sodium and aluminium are odd-Z nuclei that can be produced in massive stars, mainly during the carbon (but also neon) burning phase. ^{23}Na can also be produced by p-captures (Ne–Na cycle), and ^{27}Al can be synthesized in the same stars through the Mg–Al cycle, and accumulates for $T > 7 \times 10^7$ K. The Ne–Na and Mg–Al cycles can also occur in the deep part of the H-burning shell of low-mass stars, and these elements are among those identified as modified in the outer atmospheres of low-mass AGB stars, together with N, and O more notably.

The nearly secondary-element behaviour of aluminium in the metallicity range of our sample could be explained by the fact that this element is mainly produced by hydrostatic carbon and neon burning in massive stars, and some channels for its production come from products of ^{14}N through the CNO cycle during He burning. As a consequence, the nucleosynthesis yields of Al show a strong dependency on the metallicity of the progenitor stars. For instance,

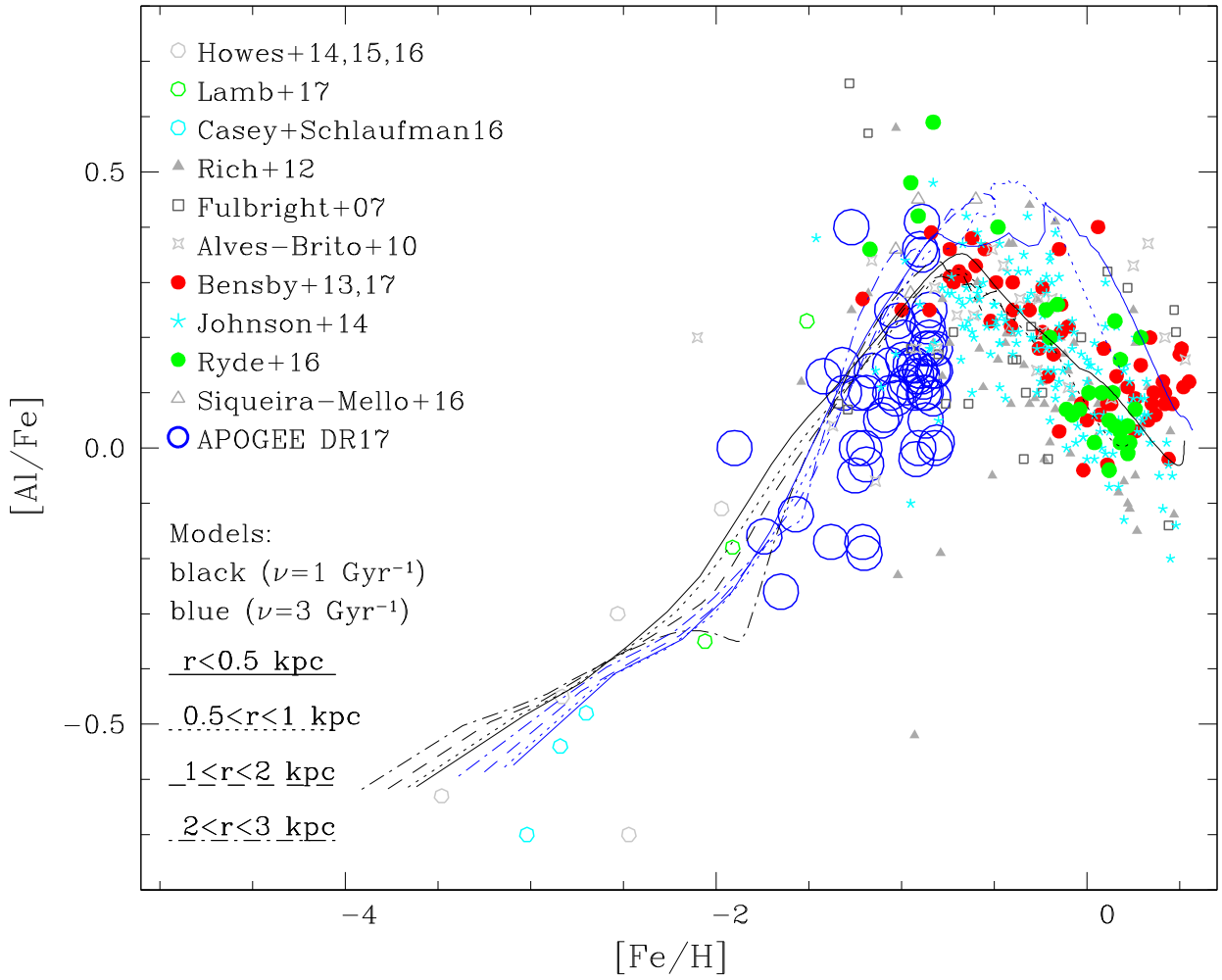

Figure 5. [Al/Fe] versus. [Fe/H] for literature bulge field stars and the APOGEE abundances (original DR17) for the 58 sample stars. Symbols: grey four-pointed stars: Alves-Brito et al. (2010); red filled circles: Bensby et al. (2017); strong-grey filled triangles: Fulbright et al. (2007); grey stars: Johnson et al. (2014); grey open pentagons: Casey & Schlaufman (2015); grey open pentagons: Howes et al. (2016); green open pentagons: Lamb et al. (2017); green filled circles: Ryde et al. (2016); grey open triangles: Siqueira-Mello et al. (2016); red open circles: APOGEE DR17 original and blue open circles were computed in this work for sample stars that had no APOGEE abundance value. Chemodynamical evolution models with SFR of $\nu = 1$ and 3 Gyr^{-1} or formation time-scale of 1 and 0.3 Gyr are overplotted.

^{22}Ne comes from ^{14}N, and gives rise to ^{27}Al, through the channel: ^{22}Ne(α,n)^{25}Mg(n,γ)^{26}Mg(p,γ)^{27}Al. In addition, the yields of ^{23}Na and ^{27}Al are both shown to depend on surplus neutrons available to the SN explosion (WW95). These nuclei behave more like secondary elements, since a significant fraction of the additional neutrons comes from stable neutron-rich nuclei that were present in the progenitor star.

The trend of [Al/Fe] versus [Fe/H] is sensitive to the SFR of the star-forming environment, getting steeper below [Fe/H] ~ -1 when star formation is faster, as we can see by comparing the models with $\nu = 1$ and 3 Gyr^{-1}. In this way, the [Al/Fe] abundance ratios could be used to constrain the formation time-scale of the system.

The SFR of 3 Gyr^{-1} corresponds to a very fast time-scale of 0.3 Gyr, whereas 1 Gyr^{-1} leads to a time-scale of 1 Gyr for the enrichment of these moderately metal-poor stars. From the [Al/Fe] versus [Fe/H] plots both time-scales appear suitable.

Finally, Fig. 6 shows the models excluding contributions from HNe (Nomoto et al. 2013), showing that the inclusion of HNe is required to satisfactorily reproduce the Al abundance in the more metal-poor bulge stars. We note that models from Kobayashi et al. (2006) decrease with decreasing metallicity, but not as steeply as needed to fit the data.

4.2 Checking for N–Na–Al correlations

Field stars in the Galactic bulge have been studied, with claims that about 8 per cent of bulge giants have enhanced [N/Fe] typical of second-generation (2G) stars evaporated from globular clusters or from disrupted globular clusters (Schiavon et al. 2017; Horta et al. 2020; Fernández-Trincado et al. 2021b, 2022b). On the other hand, Martell et al. (2016) pointed out that only a small fraction of the N-rich stars in Schiavon et al. (2017) have enhanced Al abundances typical of 2G stars.

For this reason, in Fig. 7, we plot [N/Fe] versus [Al/Fe], [Na/Fe] versus [Al/Fe], and [N/Fe] versus [Na/Fe], for all stars (red open stars), and highlight selected stars in our sample that show [Al/Fe] ≥ 0.2 (blue open stars) in order to verify correlations between N and Al, Na and Al, and N and Na. This figure indicates that there is no correlation between these abundances, which excludes these stars as being identified with originally 2G stars from globular clusters.

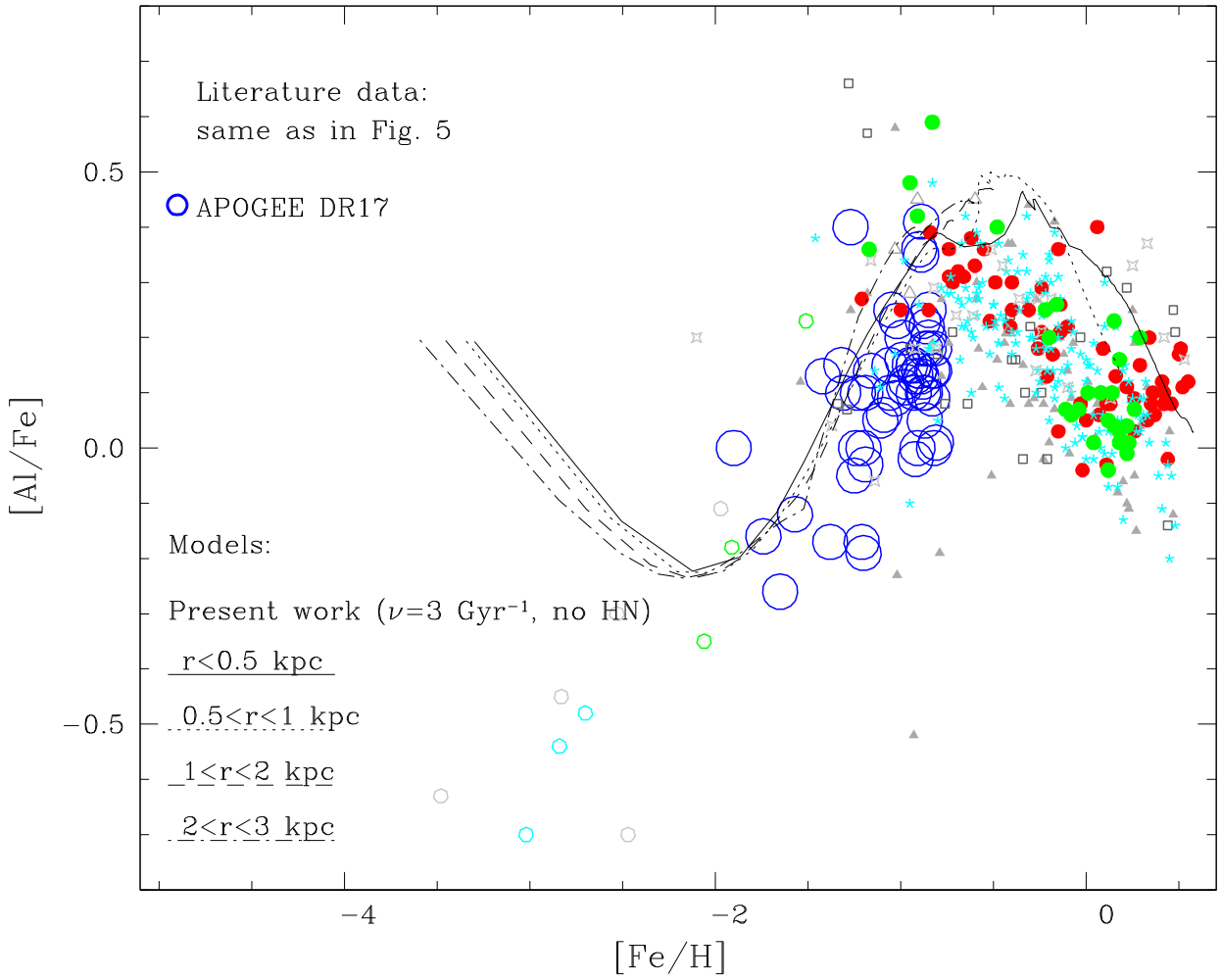

Figure 6. [Al/Fe] versus [Fe/H]: same as Fig. 5, with chemodynamical evolution models with $\nu = 3\,\mathrm{Gyr}^{-1}$ and no HNe yields overplotted.

Note that Mészáros et al. (2020) adopts [Al/Fe] $\geq +0.3$ to identify 2G stars, but we do not have many of these.

Furthermore, Fernández-Trincado et al. (2021a, 2022a) have found a correlation between Al and Ce enhancements in stars of the globular clusters NGC 6380 (Tonantzintla 1), and Tonantzintla 2 (Pismis 26). In order to check if this correlation applies to our sample, in the lower right panel of Fig. 7 is plotted [Ce/Fe] versus [Al/Fe], using Ce abundances from Razera et al. (2022) – see identification of Ce lines in Cunha et al. (2017). This figure indicates that there might be a correlation between Ce and Al enhancements, but a Pearson test shows an extremely weak correlation of a Pearson coefficient of $r = 0.08$, therefore essentially no correlation.

5 CONCLUSIONS

Razera et al. (2022) have selected 58 stars from the APOGEE list of bulge stars, as representative members of an old spheroidal bulge. For this sample, we have analysed lines of the odd-Z elements Na and Al. There are difficulties with Na lines available in the H band: in particular the apparently best line Na I 16388.850 Å appears very strong in about 20 per cent of the stars, but this Na enhancement is not confirmed by the other Na lines, and this effect was explained by Hayes et al. (2022) as due to a sky line not cancelled in the reductions, for stars in the radial velocity range of $-110 < v_r < -60\,\mathrm{km\,s}^{-1}$. For this, and also for the reason that the Na lines are shallow, ASPCAP Na abundances of only 15 stars were considered as reliable.

As concerns Al, the three rather strong and clean Al lines are very adequate for deriving Al abundances, and the results from our calculations with both TURBOSPECTRUM and PFANT confirm the ASPCAP DR17 results at least within <0.2 dex, and within <0.1 dex for most stars.

We compare the abundances of Na and Al in our sample stars to literature data for bulge stars, and to new chemodynamical model calculations. The models nicely fit the decrease of Al abundance with decreasing metallicity, and also show that it is required to have HNe included in the calculations for the metal-poor end. For Na, a spread is found in literature data as well as from the ASPCAP Na abundances. At the high-metallicity end, the data show a trend for high Na abundances, which is not reproduced by the models. This enhancement should be further investigated, to be confirmed or not, given that the interpretation of strong Na features in high-mass early-type galaxies are interpreted as a combination of high Na abundances and a top-heavy IMF (Spiniello et al. 2012), representing an important impact on stellar population studies.

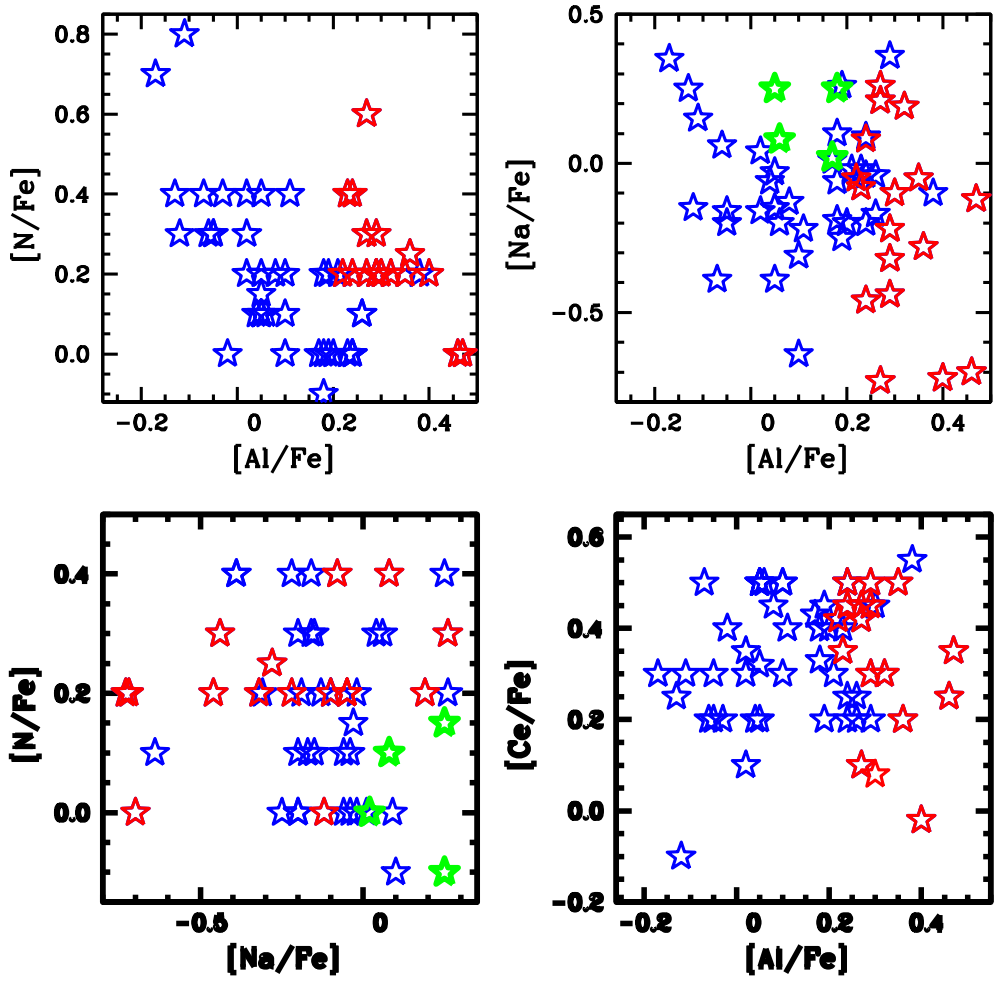

Figure 7. [N/Fe] versus [Al/Fe], [Na/Fe] versus [Al/Fe], and [N/Fe] versus [Na/Fe], and [Ce/Fe] versus [Al/Fe], plotted for all stars (blue open stars) and stars with [Al/Fe] ≥ 0.2 (red open stars), Na abundances revised in DR17 Bawlas (Hayes et al. 2017) stars (green open stars).

A moderate spread in abundances of Na and Al is not confirmed by N abundances, which exhibit no exceptional enhancement for any of the sample stars, therefore there is no evidence for these stars to correspond to 2G stars from dissolved globular clusters.

ACKNOWLEDGEMENTS

BB acknowledges grants from FAPESP, CNPq, and CAPES – Financial code 001. SOS acknowledges the FAPESP PhD fellowship no. 2018/22044-3. JGF-T gratefully acknowledges the grant support provided by Proyecto Fondecyt Iniciación no. 11220340, and from the Joint Committee ESO-Government of Chile 2021 (ORP 023/2021), and from Becas Santander Movilidad Internacional Profesores 2022, Banco Santander Chile. DG gratefully acknowledges the support provided by FONDECYT regular no. 1220264. The work of VMP is supported by NOIRLab, which is managed by the Association of Universities for Research in Astronomy (AURA) under a cooperative agreement with the National Science Foundation. MZ was funded by ANID FONDECYT Regular 1191505, ANID Millennium Institute of Astrophysics (MAS) under grant ICN12_009, the ANID BASAL Center for Astrophysics and Associated Technologies (CATA) through grants AFB170002, ACE210002, and FB210003. TCB acknowledges partial support from grant PHY 14-30152; Physics Frontier Center/JINA Center for the Evolution of the Elements (JINA-CEE), and from OISE-1927130: The International Research Network for Nuclear Astrophysics (IReNA), awarded by the US National Science Foundation.

BB, HE, TM, SOS, and PS are part of the Brazilian Participation Group (BPG) in the SDSS, from the Laboratório Interinstitucional de e-Astronomia - LIneA, Brazil. Funding for the SDSS-IV has been provided by the Alfred P. Sloan Foundation, the U.S. Department of Energy Office of Science, and the Participating Institutions. SDSS acknowledges support and resources from the Center for High-Performance Computing at the University of Utah. The SDSS web site is www.sdss.org. SDSS is managed by the Astrophysical Research Consortium for the Participating Institutions of the SDSS Collaboration including the Brazilian Participation Group, the Carnegie Institution for Science, Carnegie Mellon University, Center for Astrophysics | Harvard & Smithsonian (CfA), the Chilean Participation Group, the French Participation Group, Instituto de Astrofísica de Canarias, The Johns Hopkins University, Kavli Institute for the Physics and Mathematics of the Universe (IPMU) / University of Tokyo, the Korean Participation Group, Lawrence Berkeley National Laboratory, Leibniz Institut für Astrophysik Potsdam (AIP), Max-Planck-Institut für Astronomie (MPIA Heidelberg), Max-Planck-Institut für Astrophysik (MPA Garching), Max-Planck-Institut für

Extraterrestrische Physik (MPE), National Astronomical Observatories of China, New Mexico State University, New York University, University of Notre Dame, Observatório Nacional / MCTI, The Ohio State University, Pennsylvania State University, Shanghai Astronomical Observatory, United Kingdom Participation Group, Universidad Nacional Autónoma de México, University of Arizona, University of Colorado Boulder, University of Oxford, University of Portsmouth, University of Utah, University of Virginia, University of Washington, University of Wisconsin, Vanderbilt University, and Yale University. This work makes use of data from the European Space Agency (ESA) space mission *Gaia*. The *Gaia* mission website is https://www.cosmos.esa.int/gaia. The *Gaia* archive website is https://archives.esac.esa.int/gaia.

DATA AVAILABILITY

The observed data are from the APOGEE survey. The calculations and plots are available under request to the main author.

REFERENCES

Abdurro'uf et al., 2022, ApJS, 259, 35
Alvarez R., Plez B., 1998, A&A, 330, 1109
Alves-Brito A., Meléndez J., Asplund M., Ramírez I., Yong D., 2010, A&A, 513, A35
Arentsen A. et al., 2020, MNRAS, 491, L11
Asplund M., Amarsi A. M., Grevesse N., 2021, A&A, 653, A141
Barbuy B. et al., 2014, A&A, 570, A76
Barbuy B. et al., 2021, A&A, 648, A16
Barbuy B., Chiappini C., Gerhard O., 2018a, ARA&A, 56, 223
Barbuy B., Trevisan J., de Almeida A., 2018b, Publ. Astron. Soc. Aust., 35, 46
Barbuy B., Zoccali M., Ortolani S., Hill V., Minniti D., Bica F., Renzini A., Gómez A., 2009, A&A, 507, 405
Beaton R. L. et al., 2020, AJ, 162, 302
Belokurov V., Erkal D., Evans N. W., Koposov S. E., Deason A. J., 2018, MNRAS, 478, 611
Bensby T. et al., 2017, A&A, 605, 89
Bica E., Ortolani S., Barbuy B., 2016, Publ. Astron. Soc. Aust., 33, e028
Blanton M. R. et al., 2017, AJ, 154, 28
Brooke J. S. A. et al., 2014, ApJS, 210, 23
Casey A. R., Schlaufman K. C., 2015, ApJ, 809, 110
Chiappini C., Frischknecht U., Meynet G., HirschiR., Barbuy B., PignatariM. , Decressin T., Maeder A., 2011, Nature, 474, 666
Cunha K. et al., 2017, ApJ, 844, 145
Cunha K., Smith V. V., 2006, ApJ, 651, 491
Dékány I., Minniti D., Catelan M., Zoccali M., Saito R. K., Hempel M., Gonzalez O.A., 2013, ApJ, 776, L19
Fernández-Trincado J. G. et al., 2019, A&A, 627, A178
Fernández-Trincado J. G. et al., 2021a, ApJ, 918, L9
Fernández-Trincado J. G. et al., 2021b, ApJ, 918, L37
Fernández-Trincado J. G. et al., 2022a, A&A, 658, A116
Fernández-Trincado J. G. et al., 2022b, A&A, 663, A126
Friaça A. C. S., Barbuy B., 2017, A&A, 598, 121
Friaça A. C. S., Terlevich R. J., 1998, MNRAS, 298, 399
Fulbright J. P., McWilliam A., Rich R. M., 2007, ApJ, 661, 1152
Gaia Collaboration, 2021, A&A, 649, A1
García-Pérez A. E. et al., 2016, AJ, 151, 144
García-Pérez A. et al., 2013, ApJ, 767, L9
Goorvitch D., 1994, ApJS, 95, 535
Grevesse N., Asplund M., Sauval J. N., 2007, Space Sci. Rev., 130, 105
Grevesse N., Sauval J. N., 1998, Space Sci. Rev., 35, 161
Gunn J. E. et al., 2006, AJ, 131, 2332
Gustafsson B., Edvardsson B., Eriksson K., Jørgensen U. G., Nordlund Å., Plez B., 2008, A&A, 486, 951
Hasselquist S. et al., 2016, ApJ, 833, 81
Hayes C. R. et al., 2022, ApJS, 262, 34
Helmi A., Babusiaux C., Koppelman H. H., Massari D., Veljanoski J., Brown A. G. A., 2018, Nature, 563, 85
Horta D. et al., 2020, MNRAS, 493, 3363
Horta D. et al., 2021, MNRAS, 500, 1385
Howes L. M. et al., 2016, MNRAS, 460, 884
Iwamoto K., Brachwitz F., Nomoto K., Kishimoto N., Umeda H., Hix W.R., Thielemann F.-K., 1999, ApJS, 125, 439
Johnson C. I., Rich R. M., Kobayashi C., Kunder A., Koch A., 2014, AJ, 148, 67
Jönsson H. et al., 2020, AJ, 160, 120
Kobayashi C., Karakas A., Lugaro M., 2020, ApJ, 900, 179
Kobayashi C., Umeda H., Nomoto K., Tominaga N., Ohkubo T., 2006, ApJ, 653, 1145
Koch A., McWilliam A., Preston G. W., Thompson I. B., 2016, A&A, 587, 124
Kunder A. et al., 2020, AJ, 159, 270
Kurucz R., 1993, CD-ROM 23
Lamb M. et al., 2017, MNRAS, 465, 3536
Lecureur A., Hill V., Zoccali M., Barbuy B. , Gómez A., Ortolani S., Renzini A., 2007, A&A, 465, 799
Li G., Gordon I. E., Rothman L. S., Tan Y. , Hu S.-M., Kassi S. , Campargue A., Medvedev E. S., 2015, ApJS, 216, 15
Lucey M. et al., 2022, MNRAS, 509, 122
Majewski S. R., Schiavon R. P., Frinchaboy P. M., 2017, AJ, 154, 94
Martell S. L. et al., 2016, ApJ, 825, 146
Martin W. C. et al., 2002, Atomic, Molecular, and Optical Physics Handbook (version 1.01). National Institute of Standards and Technology, Gaithersburg, MD, [Online] Available: http://physics.nist.gov/asd
Matteucci F., Vasini A., Grisoni V., Schultheis M., 2020, MNRAS, 494, 5534
Mészáros S. et al., 2020, MNRAS, 492, 1641
Ness M. et al., 2013, MNRAS, 430, 836
Nidever D. L. et al., 2015, AJ, 150, 173
Nomoto K., Kobayashi C., Tominaga N., 2013, ARA&A, 51, 457
Nordlander T., Lind K., 2017, A&A, 607, A75
Osorio Y., Allende Prieto C., Hubeny I., Mész aros Sz., Shetrone M., 2020, A&A, 637, 80
Pérez-Villegas A., Barbuy B., Kerber L., Ortolani S, Souza S. O., Bica E., 2020, MNRAS, 491, 3251
Piskunov N., Kupka F., Ryabchikova T., Weiss W., Jeffery C., 1995, A&AS, 112, 525
Planck Collaboration VI, 2020, A&A, 641, A6
Plez B., 2012, Turbospectrum: Code for spectral synthesis, Astrophysics Source Code Library, ascl:1205.004, http://adsabs.harvard.edu/abs/2012ascl.soft05004P
Queiroz A. B. A. et al., 2018, MNRAS, 476, 2556
Queiroz A. B. A. et al., 2020, A&A, 638, A76
Queiroz A. B. A. et al., 2021, A&A, 656, A156
Razera R. et al., 2022, MNRAS, 517, 4590
Rich R. M., Origlia L., Valenti E., 2012, ApJ, 746, 59
Rojas-Arriagada A. et al., 2020, MNRAS, 499, 1037
Ryabchikova T., Piskunov N., Kurucz R. L., Stempels H. C., Heiter U., Pakhomov Y., Barklem P. S., 2015, PhyS, 90, 054005
Ryde N., Schultheis M., Grieco V., Matteucci F., Rich R. M., Uttenthaler S., 2016, AJ, 51, 1
Santana F. A. et al., 2021, AJ, 162, 303
Santiago B. X. et al., 2016, A&A, 585, 42
Savino A., Koch A., Prudil Z., Kunder A., Smolec R., 2020, A&A, 641, A96
Schiavon R. P. et al., 2017, MNRAS, 465, 501
Sestito F. et al., 2023, MNRAS, 518, 4557
Siqueira-Mello C. et al., 2016, A&A, 593, A79
Smiljanic R. et al., 2016, A&A, 589, A115
Smith V. et al., 2021, AJ, 161, 254
Sneden C., Lucatello S., Ram S. R., Brooke J. S. A., Bernath P., 2014, ApJS, 214, 26
Spiniello C., Trager S. C., Koopmans L. V. E., Chen Y. P., 2012, ApJ, 763, L32

Timmes F. X., Woosley S. E., Weaver T. A., 1995, ApJS, 98, 617
Tumlinson J., 2010, ApJ, 708, 1398
van de Hoek L. B., Groenewegen M. A. T., 1997, A&A, 123, 305
White S. D. M., Frenk C., 1991, ApJ, 379, 52
White S. D. M., Rees M. J., 1978, MNRAS, 183, 341
Wilson J. C. et al., 2019, PASP, 131, 50001
Wise J. H., Turk M. J., Norman M. L., Abel T., 2012, ApJ, 745, 50
Woosley S. E., Weaver T. A., 1995, ApJS, 101, 181, (WW95)
Yurchenko S. N., Szabo I., Pyatenko E., Tennyson J., 2018, MNRAS, 480, 3395
Zasowski G. et al., 2013, AJ, 146, 81
Zasowski G. et al., 2017, AJ, 154, 198
Zasowski G. et al., 2019, ApJ, 870, 138
Zoccali M. et al., 2017, A&A, 599, A12

[1]*IAG, Universidade de São Paulo, Rua do Matão 1226, Cidade Universitária, São Paulo, SP 05508-900, Brazil*
[2]*Lund Observatory, Department of Astronomy and Theoretical Physics, Lund University, Box 43, SE-221 00 Lund, Sweden*
[3]*Instituto de Astrofísica de Canarias, E-38205 La Laguna, Tenerife, Spain*
[4]*Steward Observatory, University of Arizona, Tucson, AZ 85719, USA*
[5]*Observatório Nacional, rua General José Cristino 77, São Cristóvão, Rio de Janeiro 20921-400, Brazil*
[6]*Institut d'Astrophysique, 98bis Bd. Arago, F-75014 Paris, France*
[7]*NSF's NOIRLab, 950 N. Cherry Ave., Tucson, AZ 85719, USA*
[8]*Universidade Federal de Sergipe, Physics Department, Av. Marechal Rondon, S/N, 49000-000 São Cristóvão, SE, Brazil*
[9]*Instituto de Astronomía, Universidad Nacional Autónoma de México, A. P. 106, C.P. 22800, Ensenada, B. C., México*
[10]*Astrophysikalisches Institut Potsdam, An der Sternwarte 16, Potsdam D-14482, Germany*
[11]*Universidad Católica del Norte, Instituto de Astronomía, Av. Angamos 0610, Antofagasta, Chile*
[12]*Universidade Federal do Rio Grande do Sul, Caixa Postal 15051, 91501-970 Porto Alegre, Brazil*
[13]*Institut de Ciències del Cosmos, Universitat de Barcelona (IEEC-UB), Martí i Franquès 1, E-08028 Barcelona, Spain*
[14]*Astrophysics Research Institute, Liverpool John Moores University, 146 Brownlow Hill, Liverpool L3 5RF, UK*
[15]*Instituto de Astrofísica, Facultad de Ciencias Exactas, Universidad Andres Bello, Fernández Concha 700, Las Condes, Santiago, Chile*
[16]*Vatican Observatory, Vatican City State, Lazio I-00120, Italy*
[17]*Departamento de Astronomia, Universidad de Concepcion, Avenida Esteban Iturra s/n Casilla 160-C, Chile*
[18]*Instituto de Investigación Multidisciplinario en Ciencia y Tecnología, Universidad de La Serena. Avenida Raúl Bitrán S/N, La Serena, Chile*
[19]*Departamento de Astronomía, Facultad de Ciencias, Universidad de La Serena. Av. Juan Cisternas 1200, La Serena, Chile*
[20]*Instituto de Astrofísica, Pontificia Universidad Católica de Chile, Vicuña Mackenna 4860, Macul, Casilla 306, Santiago 22, Chile*
[21]*Millenium Institute of Astrophysics (MAS), Nuncio Monseñor Sótero Sanz 100, Providencia, Santiago Chile*
[22]*Observatoire de la Côte d'Azur, CNRS, Laboratoire Lagrange, Université Côte d'Azur, Nice, France*
[23]*Centro de Astronomía (CITEVA), Universidad de Antofagasta, Avenida Angamos 601, Antofagasta 1270300, Chile*
[24]*University of Notre Dame, Department of Physics and Astronomy and JINA Center for the Evolution of the Elements (JINA-CEE), Notre Dame, IN 46556, USA*
[25]*Rua Waldi Kich, 535, Gramado, Rio Grande do Sul, Brazil*

This paper has been typeset from a TEX/LATEX file prepared by the author.